Research Paper

Carbon-gold hybrid nanoprobes for real-time imaging, photothermal/photodynamic and nanozyme oxidative therapy

Amin Zhang[1,2], Shaojun Pan[2,3], Yuhui Zhang[5], Jie Chang[1,2], Jin Cheng[1,2], Zhicheng Huang[1,2], Tianliang Li[1,2], Chunlei Zhang[1,2], Jesus Martinez de la Fuentea[4], Qian Zhang[1,2✉], Daxiang Cui[1,2✉]

1. Institute of Nano Biomedicine and Engineering, Shanghai Engineering Research Center for Intelligent Diagnosis and Treatment Instrument, Department of Instrument Science and Engineering, School of Electronic Information and Electrical Engineering, Shanghai Jiao Tong University, 800 Dongchuan RD, Shanghai 200240, P.R. China.
2. National Center for Translational Medicine, Collaborative Innovational Center for System Biology, Shanghai Jiao Tong University, 800 Dongchuan Road, Shanghai 200240, P. R. China.
3. School of Biomedical Engineering, Shanghai Jiao Tong University, Shanghai 200240, P. R. China.
4. Instituto de Nanociencia de Aragon (INA), Universidad de Zaragoza, Zaragoza, 50018, Spain.
5. Zhujiang Hospital, Southern Medical University, 253 Gongye Road, Guangzhou, Guangdong 510280, P.R. China.

✉ Corresponding author: E-mail address: dxcui@sjtu.edu.cn (D.X. Cui) qianzhang0130@ sjtu.edu.cn (Q. Zhang)

Abstract

Rationale: Recently, there is one-fifth of human deaths caused by cancer, leading to cancer treatment remains a hard nut to crack in the medical field. Therefore, as an emerging diagnostic technology, mesoporous nanomaterials-based drug delivery systems integrated diagnosis and therapy have aroused tremendous interest owing to visually targeting effect and superior therapy efficacy compared with traditional cancer treatment.

Methods: In this work, we have successfully synthesized mesoporous carbon-gold hybrid nanozyme nanoprobes, whereby mesoporous carbon nanospheres were doped with small gold nanoparticles (OMCAPs) and further stabilized with a complex of reduced serum albumin and folic acid (rBSA-FA). After loading IR780 iodide, the OMCAPs@ rBSA-FA@IR780 nanoprobes were finally accomplished for real-time imaging, photothermal/photodynamic and nanozyme oxidative therapy.

Results: Herein, acid oxidized MCAPs possessed large surface area and numerous –COOH groups, which could be used to surface chemically modify numerous targeting molecules and load abundant NIR dye IR780, as well as be acted as photothermal reagents to enhance photothermal therapy effect. In addition, the small Au NPs embedded in OMCAPs were utilized as nanozyme to catalyze H_2O_2 located in tumor cells to generate ·OH for intracellular oxidative damage of tumor. Besides, as a commonly used near-infrared (NIR) fluorescence dye, the loaded IR780 iodide could not only apply for real-time imaging, but also effectively enhance photo-thermal therapy (PTT) upon the 808 nm laser irradiation. Moreover, FA molecules could enhance the targeted efficiency of the nanoprobes to the gastric tumor site. According to the systematical study *in vitro* and *in vivo*, our fabricated nanoprobes based on carbon-gold hybrid (OMCAPs@ rBSA-FA@IR780) revealed excellent tumor targeting efficacy, long tumor retention and favorably therapeutic effect for tumor.

Conclusion: All the results demonstrated that here synthesized probes exhibited excellently diagnostic and therapeutic performance, indicating our technology may potentially offer an outstanding strategy for tumor-targeting theranostics.

Key words: OMCAPs, IR780, nanozyme, NIR fluorescence imaging, Photodynamic & Photothermal therapy

Introduction

In recent, extensive efforts, mainly including traditional surgery, radiotherapy, and chemotherapy, have been poured to cure cancer and reduce the death rate of cancer [1]. However, the cancer treatment is

still a hard nut to crack in the medical field, and there is one-fifth of human deaths caused by cancer. Thus, it is urgent to develop some effective invasive or noninvasive therapeutic approaches to eliminate side effects and the painfully therapeutic process causing by conventional treatment modalities. In the past decades, the emerging recognized and light-induced therapy, such as photo-thermal therapy (PTT) and photodynamic therapy (PDT) have been explored for cancer treatment [2, 3]. PTT refers to the heat generation after aborting near-infrared wavelength light when synergistically employs photothermic reagent [2, 4] due to their high tissue penetration, which could induce cancer cellular necrosis and apoptosis [5-8] with good therapeutic efficacy and minimal side-effect [9-11]. In addition, PDT is a cancer treatment based on using photosensitizers, which could form reactive oxygen species (ROS) upon laser irradiation, especially singlet oxygen ($^1O_2$) generated from transfer of the excited state energy to oxygen molecules, with a result of ablation of cancer cells [12-15]. Due to the thieir unique properties, commonly used photosensitizers including organic reagents and semiconducting polymer nanoparticles [16-18] could be applied for cancer diagnosis after photoexcitation. Therefore, the ideally utilized photothermic reagent should display strong absorbance in NIR range (700-900 nm) and effectively transfer optical energy into heat energy with low toxicity and high aggregation of tumor sites [19]. Additionally, the desired photosensitizers should be with perfect pharmacokinetics [20]. Considering the factors mentioned above, NIR dyes IR-780 iodide, a lipophilic cation heptamethine dye possessed high quantum yield, low tissue autofluorescence, deep tissue penetration, real-time image-guided property and favorable stability [1, 21], could be a promising candidate in the application of tumor imaging, diagnosis and targeted therapy.

Currently, designing and synthesizing various kinds of artificial enzymes have aroused alternatives numerous attention, which are nanomaterials possessed intrinsic enzyme-like activity and acted as promising alternatives to nature enzymes [22]. Compared with natural enzymes, artificial enzymes own many a merit including low cost, ease-constructed process, favorable stability and long-time storage, especially the shape- and size-dependent enzymatic catalysis [23, 24]. As a crucial branch of biomimetic chemistry [25], nanozymes mainly contain metal nanomaterials [24, 26], carbon nanomaterials [27], semiconducting polymer [28, 29] and metal-organic frameworks [30], and they have exhibited eminent potential advantages in various fields of biomedicine and biosensors' construction

[31], with several applications including sensing, imaging and therapeutics and so forth. In some systems, the developed nanozymes could catalyze the hydrogen peroxide (H_2O_2) plentifully located in the tumor site to generate ROS, and further destroy the harmful tumor organisms without damaging normal cells. Notably, ROS including superoxide radicals and hydroxyl radicals could cause cells apoptosis or necrosis when ROS was at an abnormal level. For instance, gold nanoparticles (Au NPs) are one of most researched nanozymes which possess peroxidase-mimic activity and could perform ROS regulation, in which Au NPs could generate hydroxyl radicals at acidic microenvironments in the presence of hydrogen peroxide (H_2O_2) to make cell apoptosis and ablate tumor [32-34]. Therefore, effectively utilizing the special microenvironment of tumors such as high H_2O_2 concentration level and acid circumstance is an applicable and promising strategy for tumor therapy by synergistically using nanozymes' strong oxidizing ability.

Carbon-based nanomaterials have received tremendous attention owing to their superior physico-chemical properties, such as long-term stability, favorable conductivity and high specific surface area. Commonly used carbon nanomaterials cover carbon nanotubes (CNT), graphene oxide (GO) and carbon nanospheres (CNPs) and so forth. With unique advantages of uniform size, large pore volume, good biocompatibility, excellent electrical conductivity and favorable heat generation under efficient UV–Vis–NIR light absorption [35-37], mesoporous carbon nanospheres (MCNs) are extensively applied in biomedicine field [38, 39], biochemical assay [40] and immunoassay [41, 42]. Moreover, previous studies reported that MCNs were NIR-resonant nanomaterials and always used as drug carrier used for chemo-photothermal therapy [36, 38, 39, 43-47]. Inspired by all features of MCNs and nanozymes, we synthesized the carriers which were MCNs doped small Au NPs (MCAPs), where the pores were open and little Au NPs were intercalated into mesostructures instead of being adhered to the outside of carbon shell. Notably, the constructed MCAPs had good porosity to immobilize abundant fluorescent substance, excellent surface chemistry to modify target molecule and good light-absorbing ability to PPT therapy. Specifically, intercalated Au NPs in the MCAPs could be utilized as nanozyme for synergistic cancer therapy. Interestingly, intercalated Au NPs could be prevented aggregation by surface-generated carbon nanomaterial in absence of any surfactants, to accomplish the effectively enhancing stability and catalytic activity.

Through the rational design process, this study

we constructed MCNs via a hydrothermal process and doped small Au NPs inside to form MCAPs. Then, the MCAPs were further treated with strong sulfuric and nitric acid to produce abundant carboxyl groups on their surfaces (OMCAPs) for hydrophilicity enhancement. According to the covalent coupling via EDC chemistry, target molecule rBSA-FA could be modified on the surface of OMCAPs, and then physical loaded NIR dyes IR-780 iodide to finally fabricate multifunctional OMCAPs@rBSA-FA@IR780 nanoprobes. These probes could multirole such as being NIR fluorescent probe for tumor imaging, the photosensitizer for cancer PDT therapy, the nanozyme for cancer therapy and photothermal reagent for PTT therapy (details are shown in Scheme 1). In this work, novel OMCAPs@rBSA-FA@IR780 nanocomposites have successfully prepared for gastric cancer tumor diagnosis, nanozyme analysis, PTT & PDT therapy. The developed nanocomposites owned a favorable catalysis ability, NIR fluorescent imaging properties, and good tumor targeted-therapy capacity in MGC803 tumor-bearing mice, which would pave a potential way for designing a novel approach in cancer diagnosis and treatment.

Results and Discussion

Preparation and characterization of OMCAPs@rBSA-FA@IR780

In this work, the superficial morphologies and structure information of various materials containing MCAPs, OMCAPs, OMCAPs@rBSA-FA and OMCAPs@rBSA-FA@IR780 nanoprobes were characterized by transmission electron microscopy

(TEM) and scanning electron microscopy (SEM), respectively. As displayed in Fig. 1A, the three-dimensional sphere structure of MCAPs could be clearly observed, in which the ordered mesopores and small Au NPs could be obviously distinguished under the high-resolution transmission electron microscope (HR-TEM), indicating high loading capacity and enzymatic catalytic capacity of synthesized MCAPs. The core size distribution of MCAPs was calculated from TEM image using Image J shown in Fig. S1A, with a result of ca.100 nm. In addition, HAADF-STEM was employed to identify Au NPs clearly, in which metallic Au NPs with high electronic density could be obviously observed (Fig. 1B). Moreover, the EDX elemental mapping effectively exhibited the distribution of gold and carbon elements (Fig. 1C). SEM image in Fig. 1D further showed that the obtained MCAPs were uniform with a sphere structure. To enhance the hydrophilicity and improve the surface chemical activity, the acquired MCAPs were acidized with strong acid mixture to form numerous –COOH at the surface of OMCAPs. Then, the OMCAPs were modified with rBSA-FA and following loaded NIR dye IR780. The morphologies during the fabrication process were further investigated by TEM (Fig. 1E-G). OMCAPs after acidizing remained the spherical shapes and the small ordered mesoporous (Fig. 1E), while abundant of mesopores were disappeared in OMCAPs@rBSA-FA (Fig. 1F), indicating successfully immobilized rBSA-FA at the surface of OMCAPs caused the disappearance of superficial pores. From Fig. 1G we could clearly visualize that the pores were almost disappeared owing to that loading IR780
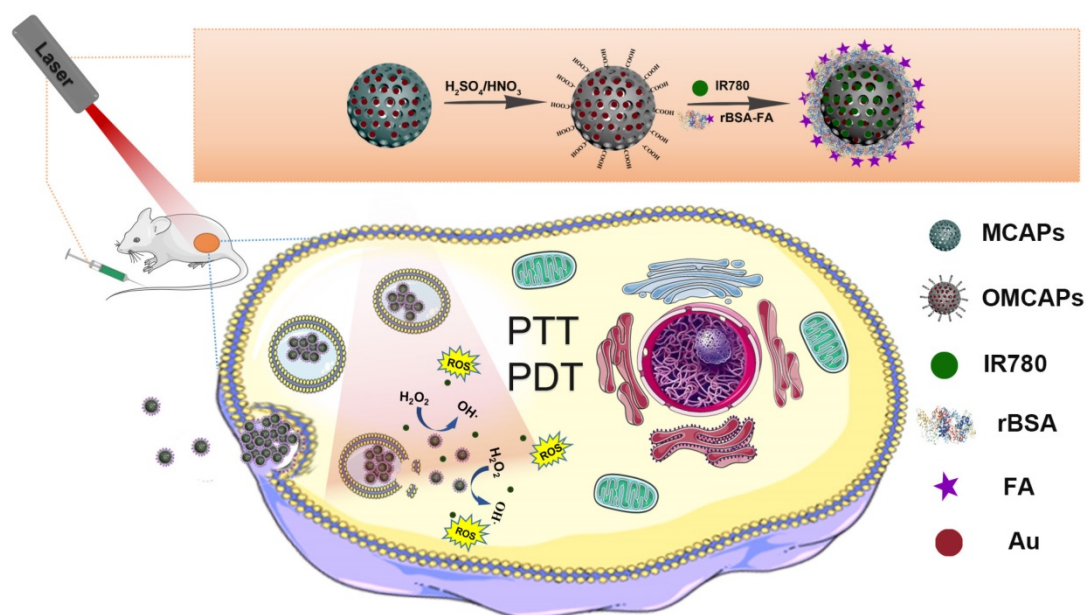
Scheme 1. Schematic diagram for construction procedure of OMCAPs@rBSA-FA@IR780 and their therapy application *in vivo*.

blocked the pores, indicating that the dye IR780 were successfully stowed in the inner of OMCAPs@rBSA-FA. Moreover, based on the calibration curve between intensity and IR780 concentrations (Fig. S3), the EE and LR of used IR780 were reached to 83.3% and 33.3 % in respective, indicating the favorable loading ability of OMCAPs.

In addition, the hydrodynamic sizes of OMCAPs, OMCAPs@rBSA-FA and OMCAPs@rBSA-FA@IR780 were illustrated in Fig. 1 H, with the result of 175.54, 177.69 and 218.71 nm, respectively. With the step-by-step modification of the probes, the sizes were increased progressively due to the attachment of rBSA-FA layer and the hydrophobic effect of doped IR780. Moreover, the zeta potential values of OMCAPs, OMCAPs@rBSA-FA and OMCAPs@rBSA-FA@IR780 were calculated as -20 mV, -47 mV and -28 mV (Fig. S1B). Likewise, the stability was studied by measuring the hydrodynamic diameters over time (shown in Fig. 1I); the material OMCAPs, OMCAPs@rBSA-FA and OMCAPs@rBSA-FA@IR780 in water have consistent size up to 4 weeks, indicating the favorable stability of the finally synthesized probes.

UV-vis spectroscopy and Fourier Transform infrared spectrum (FTIR) were respectively employed to testify the success of systematic immobilization. As shown in Fig. 2A, OMCAPs (curve a) displayed a typical absorption peak at 235 nm which might be corresponded to the π-π* transition of aromatic domains in the synthesized OMCAPs [48]. In addition, the composites rBSA-FA (curve b) exhibited two specific peaks at 280 nm and 346 nm owing to the absorption of rBSA and FA respectively. To certify that BSA connected with FA successfully, the detail UV-vis and infrared information of rBSA and FA was demonstrated in supporting information (Fig. S2A-B). Compared with bared OMCAPs (curve a), there was an additional peak at 348 nm (curve c) owing to the existence of FA and a red-shifted peak at 260 nm owing to the superposition of the UV-vis absorption from OMCAPs and rBSA. Due to the typical absorption peak at 776 nm of IR780 molecules (curve d), there was a strong and broad specific absorption peak appeared from 600 to 900 nm in the IR780 loaded OMCAPs@rBSA-FA (curve e), with an obviously red-shifted from 776 to 804 nm owing to the aggregation of IR780 in the inner of OMCAPs, indicating the successful loading of IR780 and favorable stability of loaded IR780. Additionally, FTIR was also applied for investigating the fabricated process. As showed in Fig. 2B, bare OMCAPs (curve a) exhibited an obvious infrared peak at 1631 cm^{-1} owing to the formation of abundant -COOH groups.

The complex of rBSA-FA showed a specific peak at 1656 cm^{-1} (curve b) relying on the generation of ester bond by crosslinking rBSA and FA. In addition, the peaks in curve b including 1545 cm^{-1}, 1446 cm^{-1}, 1398 cm^{-1} and 1339 cm^{-1} might due to the vibration from a benzene ring of FA. Thus, the OMCAPs@rBSA-FA exhibited the specific peaks of benzene at 1514 cm^{-1} and 1339 cm^{-1} (curve c) compared with the bare OMCAPs. Moreover, the NIR molecule IR780 (curve d) displayed specific IR peaks at 1632 cm^{-1}, 1515 cm^{-1}, 1402 cm^{-1} due to the stretching vibration of C=C in benzene ring, and 1252 cm^{-1} rely on the stretching vibration of C-H from the benzene ring. Therefore, when the small IR780 molecules were loaded into inner of OMCAPs@rBSA-FA (curve e), there were additional 1252 cm^{-1} IR specific peak according to the existence of IR780, indicating the successful step-by-step preparation of OMCAPs@rBSA-FA@IR780.

Mimicking Enzymatic Activities

The peroxidase-like activity of obtained OMCAPs and OMCAPs@rBSA-FA nanoprobes could be testified by catalyzing the oxidation of peroxidase substrate tetramethylbenzidine (TMB). As shown in Fig. 2 C, there was no obvious oxidation effect for H$_2$O$_2$ in absence of nanomaterials (control group). After adding OMCAPs (curve b) or OMCAPs@rBSA-FA (curve c), TMB has a significantly absorption peak at 652 nm in presence of H$_2$O$_2$, indicating the nanoenzyme activities of nanomaterials. Moreover, both of them exhibited the consistent catalysis efficiency, suggesting a layer of rBSA-FA had no obviously influence for the internal catalytic capacity of Au NPs. In addition, time-dependent absorbance changes at 652 nm under various pH values were displayed in the inset of Fig. 2C, we could find that OMCAPs@rBSA-FA possessed peroxidase mimetic activity over a broad pH (4.5-6.0) range and acidic environment was benefited to probes' peroxidase-like activity. Here demonstrated peroxidase-like activity of OMCAPs@rBSA-FA was similar to catalysis ability of horseradish peroxidase (HRP) and could perform ROS regulation, which might be mainly attributed to the existence of small Au NPs doped in the OMCAPs@rBSA-FA. Besides, the significant fluorescence enhancement of 2-hydroxy terephthalic acid could be observed in presence of OMCAPs or OMCAPs@rBSA-FA (Fig. 2D), indicating the generation of ·OH. All results indicated that the inner Au NPs could be performed as nanozymes to produce hydroxyl radicals for cancer oxidative therapy.
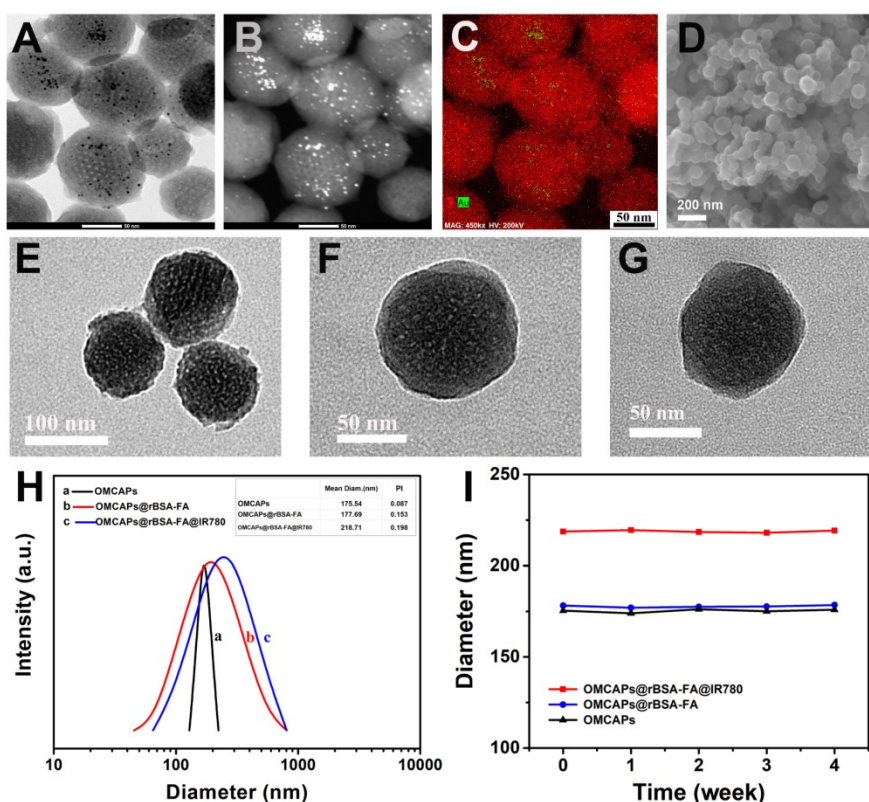
Figure 1. (A) High resolution transmission electron microscopy (HR-TEM) image, (B) HAADF-STEM pictures of MCAPs and (C) The EDX elemental mapping images of Au NPs doped MCAPs. (D) SEM image of MCAPs. (E-G) TEM images, (H) hydrodynamic diameter and (I) stability study of OMCAPs, OMCAPs@rBSA-FA and OMCAPs@rBSA-FA@IR780.
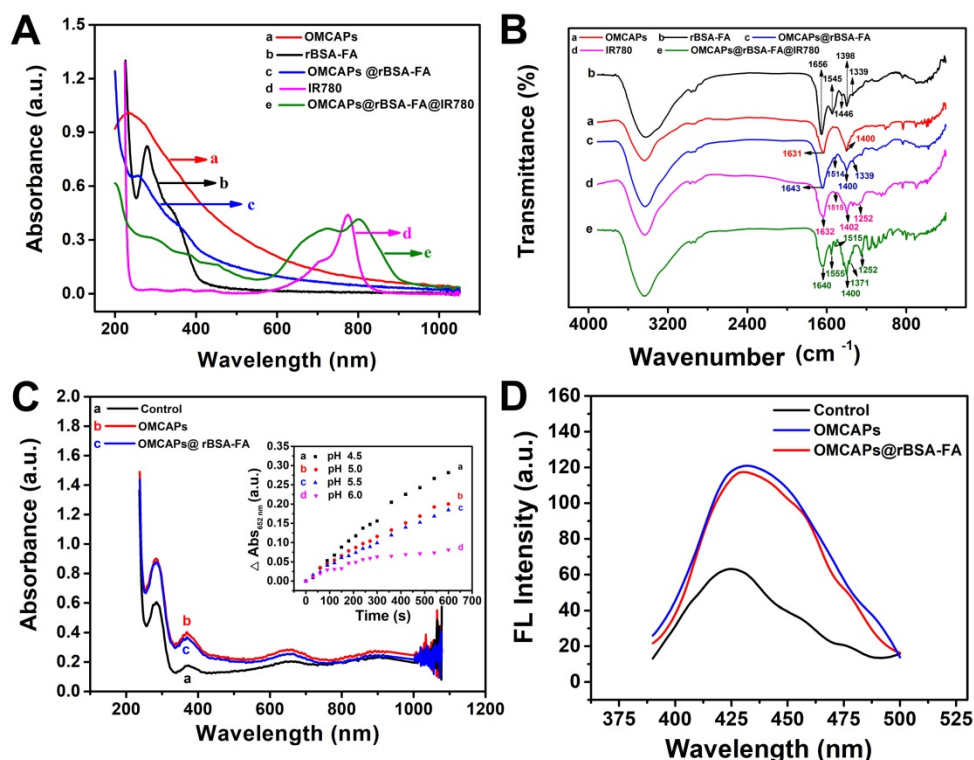

Figure 2. (A) UV-vis spectra and (B) FTIR of (a) OMCAPs, (b) rBSA-FA, (c) OMCAPs@rBSA-FA, (d) free IR780 and (e) OMCAPs@rBSA-FA@IR780. (C) UV-vis spectra of TMB in various reaction systems: (a) TMB + H_2O_2 (control), (b) TMB + H_2O_2 + OMCAPs and (c) TMB + H_2O_2 + OMCAPs@rBSA-FA in NaAc buffer (pH 6.0) after 10 min reaction. Inset: Time-dependent absorbance changes at 652 nm of TMB + H_2O_2 + OMCAPs and OMCAPs@rBSA-FA with various pH conditions. The concentrations of TMB, H_2O_2, OMCAPs and OMCAPs@rBSA-FA were 0.416 mM, 100 µM, 10 µg/mL and 10 µg/mL, respectively. (D) The determination of ·OH by recording fluorescence spectra of H_2O_2 + TA (control), H_2O_2 + OMCAPs + TA and H_2O_2 + OMCAPs@rBSA-FA + TA.
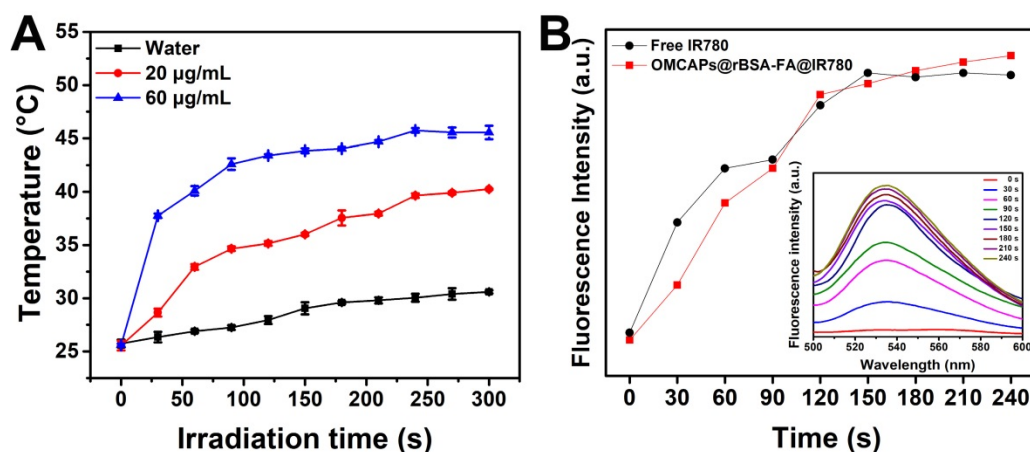
Figure 3. (A) Temperature variation of OMCAPs@rBSA-FA@IR780 (20, 60 μg/mL of contained IR-780) under 808 nm laser irradiation (1.0 W/cm²) during 300 s, water was used as control (n=3). (B) SOSG fluorescence for determination of singlet oxygen ($^1O_2$) generation of free IR780 and OMCAPs@rBSA-FA@IR780 under laser irradiation. The inset: fluorescence curves of SOSG after various irradiation time.

PTT and PDT study of nanoprobes *in vitro*

In order to evaluate the photothermic efficiency of fabricated OMCAPs@rBSA-FA@IR780 nanoprobes, the temperature fluctuation at different time point of various systems have been *in vitro* monitored under 808 nm laser irradiation with 1.0 W/cm² within 300 s. As exhibited in Fig. 3A, the control group presented a slight temperature change, while the temperature of nanoprobes (20 and 60 μg/mL of IR-780) showed obvious changes from 25 to 40 °C and 25 to 45°C respectively. This indicated that heat generation was proportional to the IR780 dosage under illumination, and the potential and favorable PTT efficacy of OMCAPs@rBSA-FA@IR780 can cause irreversible PTT damage for tumor and realize cancer therapy. The high temperature changes of OMCAPs@rBSA-FA@IR780 would be attributed to favorable heat generation under efficient UV–Vis–NIR light absorption of OMCAPs and good photothermal effect of IR780.

In order to investigate the PDT properties of constructed nanoprobes, especially the generation of singlet oxygen, the SOSG fluorescence in the aqueous solution at various time point by adding free IR780 (50 μg/mL) or OMCAPs@rBSA-FA@IR780 (equivalent to 50 μg/mL IR780) were quantitatively recorded in presence of 2.5 ×10⁻⁶ M SOSG reagent upon 808 nm laser irradiation (1.0 W/cm²). As showed in Fig. 3B, both free IR780 and the nanoprobes produced almost consistent singlet oxygen amount at the same dosages, and reached the maximum values after a few minutes. Moreover, the corresponded SOSG fluorescence spectrum of OMCAPs@rBSA-FA@IR780 probe depend on irradiation time were inserted into to the Fig. 3B, revealing that the PDT effect of nanoprobes was increased with irradiated times.

Cellular uptake and intracellular distribution

The interacted circumstances and intracellular distribution at different periods between MGA-803 cells and various materials (free IR780 and OMCAPs@rBSA-FA@IR780) were investigated by a confocal laser scanning microscopy (CLSM) and flow cytometry (FC) (Fig. 4 A-B). As shown in Fig. 4A, the red fluorescence intensity of IR780 in MGC-803 cells were gradually enhanced over time. Owing to the targeting effect of FA at the surface of OMCAPs@rBSA-FA@IR780, the fluorescence intensity treated with nanoprobes was significantly higher than that with free IR780. To further investigate the effect of FA on the targeting ability of nanoprobes, the CLSM was carried out to detect the red fluorescence of cells after incubated with OMCAPs@rBSA@IR780 and OMCAPs@rBSA-FA@IR780 at various time point. From the Fig. S6A we could find that the red fluorescence intensity was gradually increased over time. In addition, the red fluorescence intensity collected from OMCAPs@rBSA-FA@IR780 treated cells was stronger that the group without FA, indicating the FA occupied a significant role in targeting process of probes. Additionally, the median fluorescence values over time were calculated by flow cytometry, as displayed in Fig. 4B, the fluorescence intensity was gradually increased, and the values of free IR780 and nanoprobes at 12 h reached to 550 and 717, respectively. All observations discussed here indicated that FA ligands immobilized on the surface of OMCAPs@rBSA-FA@IR780 could improve specific target and the constructed OMCAPs@rBSA-FA might offer an outstanding strategy for transporting numerous dye IR780 molecules into the specific tumor cells.
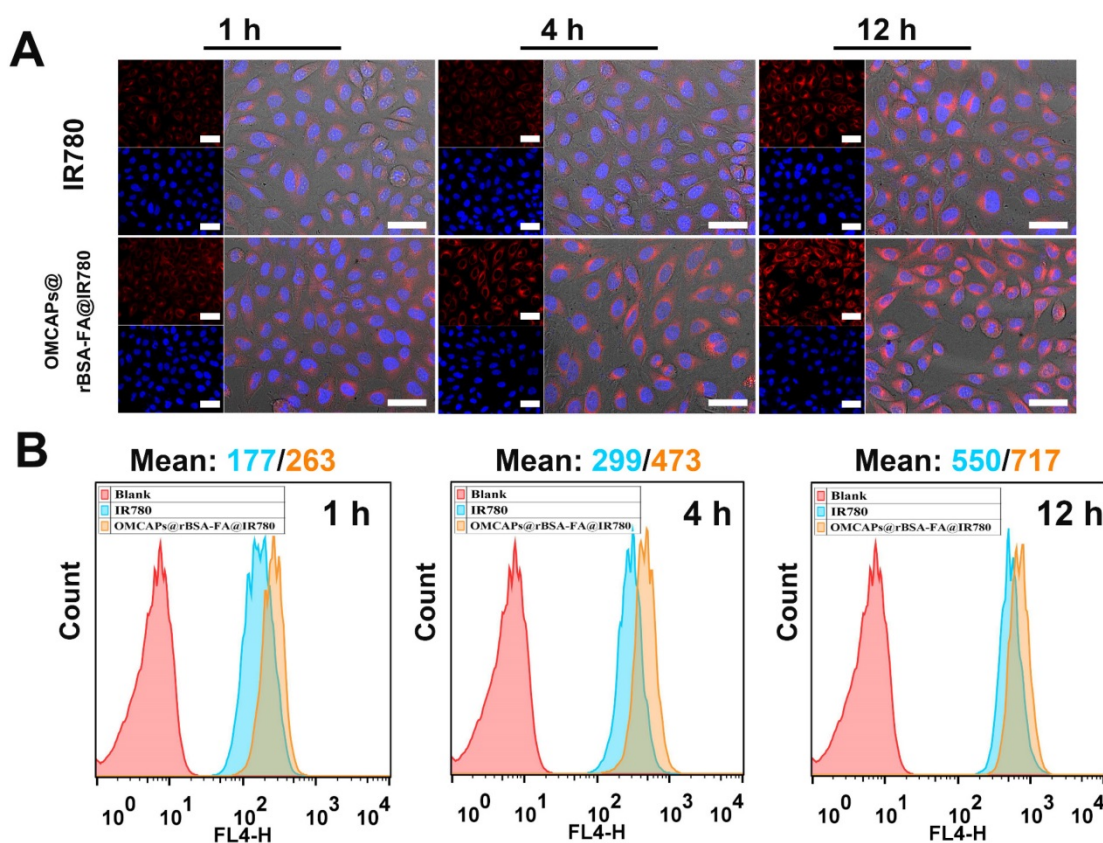
Figure 4. Cellular uptake and distribution study. (A) Confocal images of MGC-803 cells interacted with free IR780 and OMCAPs@rBSA-FA@IR780 at different times (1, 4 and 12 h). The red fluorescence revealed the existence of IR780 and the blue fluorescence was caused by DAPI dye, which was used to reflect location of cell nuclei. Scale bar: 50 μm. (B) The corresponding time point of Flow cytometry analysis of the cellular uptake.

In vitro cell toxicity

IR780 release from OMCAPs@rBSA-FA@IR780 was investigated with incubation of MCG-803 cells. As revealed in Fig. 5A, the fluorescence signal was enhanced with incubation time between OMCAPs@rBSA-FA@IR780 and MGC-803 cells. In contrast, there was no fluorescence intensity change observed over time when the nanoprobes were dissolved in culture medium in absence of cells. These results demonstrated that OMCAPs@rBSA-FA@IR780 probes were stable in the culture medium without dye IR780 releasing, which resulted in fluorescence self-quenching of IR780 in the inner of OMCAPs@rBSA-FA. Once the nanoprobes were uptake into the tumor cells, IR780 dye might be slowly released due to specifically low pH environment of cancer cells and effect of bio-enzyme in lysosomes on destruction of surficial BSA layer, resulting a distinct fluorescence enhancement of IR780 with the increment of incubation time.

The photo-toxicity and cellular proliferation inhibition by free IR780, OMCAPs@rBSA-FA and OMCAPs@rBSA-FA@IR780 were quantified by CCK-8 assay. From Fig. 5B we could observe that obvious difference between the laser irradiated group and dark group. The groups included free IR780, OMCAPs@rBSA-FA and OMCAPs@rBSA-FA@IR780 (IR780 dosage: 0-6 μg/mL, OMCAPs@rBSA-FA dosage: 0-12 μg/mL) showed favorable biocompatibility to MGC-803 cells in absence of laser irradiation. However, upon with laser irradiation, the survival rate of cells distinctly performed a concentration-dependent decrease. Notably, the survival rate of cells treated with OMCAPs@rBSA-FA@IR780 was much lower than that with free IR780 or OMCAPs@rBSA-FA, and the survival rate could down to 20 % when the concentration of IR780 in OMCAPs@rBSA-FA@IR780 turned to 6 μg/mL. In addition, the inhibitory concentration (IC_{50}) value of the OMCAPs@rBSA-FA@IR780 could be calculated as a low concentration with 9.9 μg/mL when the cells were treated with laser irradiation, indicating excellent therapeutic effect of probes. All above-acquired results might be attributed to superiorly synergistic PTT effect of IR780 and OMCAPs of nanoprobes, the favorable specifically targeted effect of OMCAPs@rBSA-FA@IR780 as well as the synergistic catalysis therapy of nanozyme Au NPs. To testify synergistic catalysis therapy of Au NPs and the PDT therapy of IR780, intracellular ROS

generation of various materials under dark or laser treatment was analyzed and the H_2DCFDA dye was employed to stain cells. As shown in Fig. S6B, compared with groups of PBS and IR780, slight green fluorescence could be observed in the cells after treated with OMCAPs@rBSA-FA and OMCAPs@rBSA-FA@IR780 in absence or presence of laser, indicating internal Au NPs act as nanozymes to produce ROS in the cells in any conditions. However, green fluorescence from cells incubated with IR780 could only be detected after laser irradiation, suggesting that IR780 could generate ROS under irradiation. Due to the synergistic effect of IR780 and OMCAPs@rBSA-FA, we could find that the strongest green fluorescence was detected in the cells after treatment with OMCAPs@rBSA-FA@IR780, revealing their excellent abilities for ROS production under irradiation.

To obviously exhibit the cellular ROS generation efficiency of OMCAPs@rBSA-FA, investigation of ROS production was accomplished by co-incubation the MGC-803 cells with OMCAPs@rBSA-FA at various concentration from 5 to 30 µg/mL, which were recorded by a laser scanning confocal microscopy. As shown in Fig. S5, the OMCAPs@rBSA-FA nanoprobes were possessed favorable biocompatibility even the concentration reached to 30 µg/mL, and the ROS level is proportional to the added concentration of OMCAPs@rBSA-FA, suggesting the probes exhibited excellent nanozyme oxidative therapy effect after targeted enrichment at the tumor site.

In this work, flow cytometry was also employed to evaluate *in vitro* antitumor efficacy of the cells after interaction with free IR780, OMCAPs@rBSA-FA and OMCAPs@rBSA-FA@IR780 with or without laser irradiation (IR780 dosage: 6 µg/mL, OMCAPs@rBSA-FA dosage: 12 µg/mL). Herein, Annexin V-FITC and propidium iodide (PI) dual labeling were used to stained dead and live cells. As shown in Fig. 5C, there was no significant decrease of the cell viability after treated with PBS in absence or presence of laser, indicating that the laser power remained within safe limits. In addition, the cell viabilities treated with free IR780, OMCAPs@rBSA-FA and OMCAPs@rBSA-FA@IR780 in dark were almost as same as that treated with PBS, suggesting that the concentration of various materials used here were safe and favorable biocompatibility of synthesized materials. However, the cells incubated with free IR780, OMCAPs@rBSA-FA and OMCAPs@rBSA-FA@IR780 under laser irradiation induced obvious cell apoptosis, and the therapy efficiency of OMCAPs@rBSA-FA@IR780 was distinctly higher than free IR780 and OMCAPs@rBSA-FA treated cells. All results detected in flow cytometry reconfirmed the observation in CCK-8 assay.

Moreover, calcein-AM and PI staining method was applied for visually revealing the photo toxicity of free IR780, OMCAPs@rBSA-FA and OMCAPs@rBSA-FA@IR780 after 5 min laser irradiation, respectively. As exhibited in Fig. 5D, there were almost no dead cells observed in the dark groups, indicating the good biocompatibility of the samples. However, compared to the weak red fluorescence treated with free IR780 and OMCAPs@rBSA-FA under laser exposure, a distinctly red fluorescence signal appeared in the cells exposed with OMCAPs@rBSA-FA@IR780 nanoprobes, indicating that they had stronger phototoxicity and better phototherapy effect. In a word, all the above-mentioned results were consistent to reveal that OMCAPs@rBSA-FA@IR780 nanoprobes displayed a remarkable therapeutic efficacy due to high loading ability of OMCAPs, good targeting ability of rBSA-FA, favorable catalysis ability of gold nanozyme, PDT effect of IR780 as well as the synergetic PTT effect of IR780 and OMCAPs.

In vivo tumor-targeted fluorescence imaging evaluation

In vivo tumor-targeted fluorescence images of free IR780 and OMCAPs@rBSA-FA@IR780 nanoprobes were carried out on an optical imaging technique, and the tumor-targeting capabilities of various materials were investigated based on the real-time distribution in mice after tail vein injection. As shown in Fig. 6A, there was no obvious fluorescence signal observed in the pre-injection mice. After 2 h post-injection, the tumor site of the OMCAPs@rBSA-FA@IR780 treated mice presented obvious fluorescence signal compared with free IR780 group, indicating the good tumor-targeting capabilities of modified FA on the surface of nanoprobes. With prolonging the circulation time, the fluorescence intensity observed in the tumor site kept enhanced, and there was still a strong red fluorescence up to 48 h, which was due to the gradual release of IR780 in the tumor environment. In contrast, the fluorescence signal of free IR780 treated mice distributed the whole body and mainly revealed in liver while the signal in tumor site was relatively weak due to the absence of targeting molecule folic acid. Moreover, the signal of free IR780 treated mice reached to a maximum value at 12 h and decreased after 24 h post-injection owing to fast metabolism of small IR780 molecules.
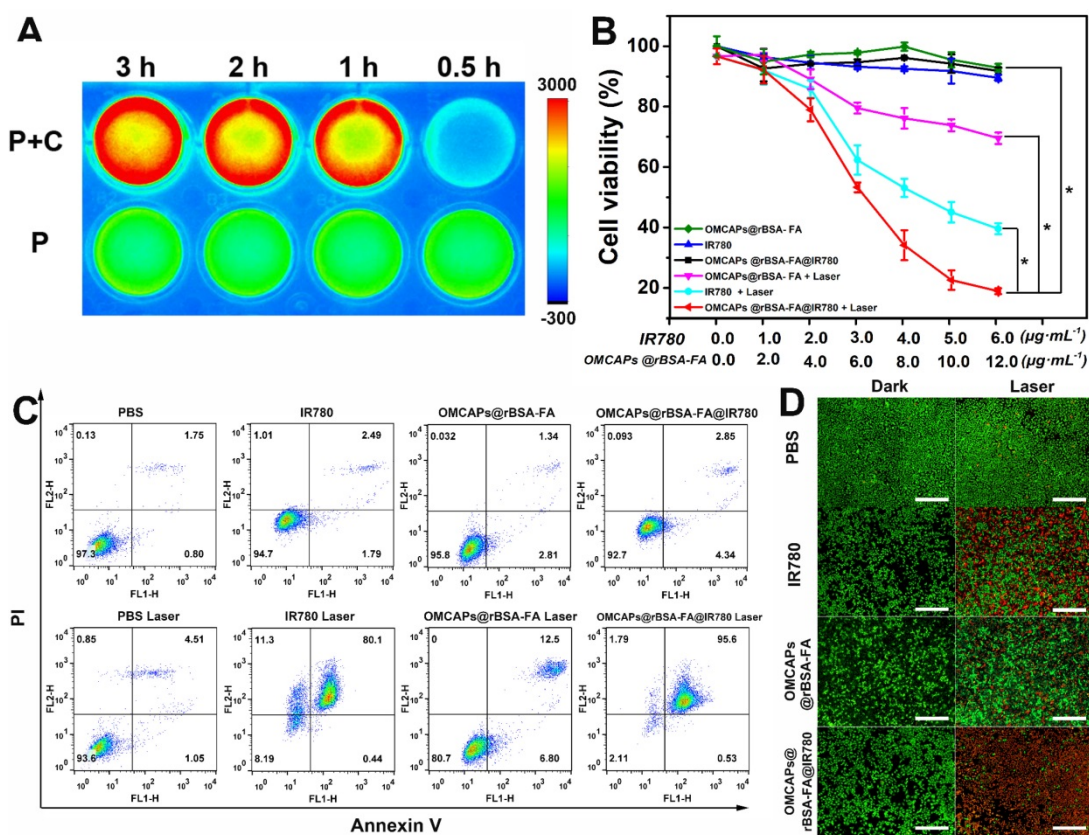
Figure 5. (A) The NIR imaging of OMCAPs@rBSA-FA@IR780 in culture medium incubated with (P+C) or without MGC-803 cells (P) at different point. *In vitro* cell toxicity assay: (B) CCK-8 assay (n=5, *P < 0.05), (C) flow cytometry and (D) fluorescence microscopy for detection of dark toxicity and photo toxicity from PBS (control), free IR780, OMCAPs@rBSA-FA and OMCAPs@rBSA-FA@IR780 (in Fig. 5D calcine PI and calcine AM stained cells, red fluorescence of PI represented dead cells while green fluorescence of calcine AM revealed live cells). Scale bar: 500 μm.

Furthermore, the fluorescence intensity at tumor sites were quantitatively calculated as illustrated in Fig. 6B. The mean fluorescence value of OMCAPs@rBSA-FA@IR780 treated mice could reach to 5000, which was about 2-fold higher than free IR780 after 24 h circulation in the mice body. Moreover, there was no obvious decrement detected at 36 h and even to 48 h, revealing the long detention time and excellent targeting ability of constructed nanoprobes. To further prove long detention time of nanoprobes, the blood circulation time of nanoprobes was detected. According to the Fig. S4 and Fig. S7, we could calculate that the blood circulation half-lives reached to 12.08 ± 1.5 h, showing long retention time of the prepared nanoprobes, due to the large size (ca. 100 nm) prevent the fast clearance of constructed nanoprobes.

To testify the body-distribution of OMCAPs@rBSA-FA@IR780 nanoprobes, the fluorescence images of excised tumor and main organs (heart, liver, spleen, lungs and kidney) from the nanoprobes treated mice were obtained at different time points (1, 12, 24 and 48 h) after post-injection. As shown in Fig. S10, there was no obvious fluorescence signal observed in main organs

at various time points. However, a strong red fluorescence could be found in tumor site of nanoprobes treated mice at 12, 24 and 48 h, indicating long detention time of nanoprobes. To clearly distinguish the body-distribution of free IR780 and prepared nanoprobes, the *ex vivo* confocal images of main organs and tumor by IR780 and nanoprobes treated mice were obtained after 48 h post-injection. As showed in Fig. 6C, there was a stronger fluorescence signal appeared in the tumor of OMCAPs@rBSA-FA@IR780 treated mice while a relatively weak signal exhibited in the tumor of free IR780 treated mice, which once proved the favorable *in vivo* tumor-targeted ability of constructed nanoprobes. In addition, there was no obvious signal observed in other organs of nanoprobes treated mice, yet a clear accumulation in the lungs of free IR780. This might be because the free IR780 molecules would be agglomerated due to their strong hydrophobicity after intravenous injection, and then entrapped in the lung of mice. In contrast, there was no obvious fluorescence observed in the lung of probes treated mice, suggesting their favorable biocompatibility. This result indicated that the nanopobes had excellent safety and tumor targeting effect.
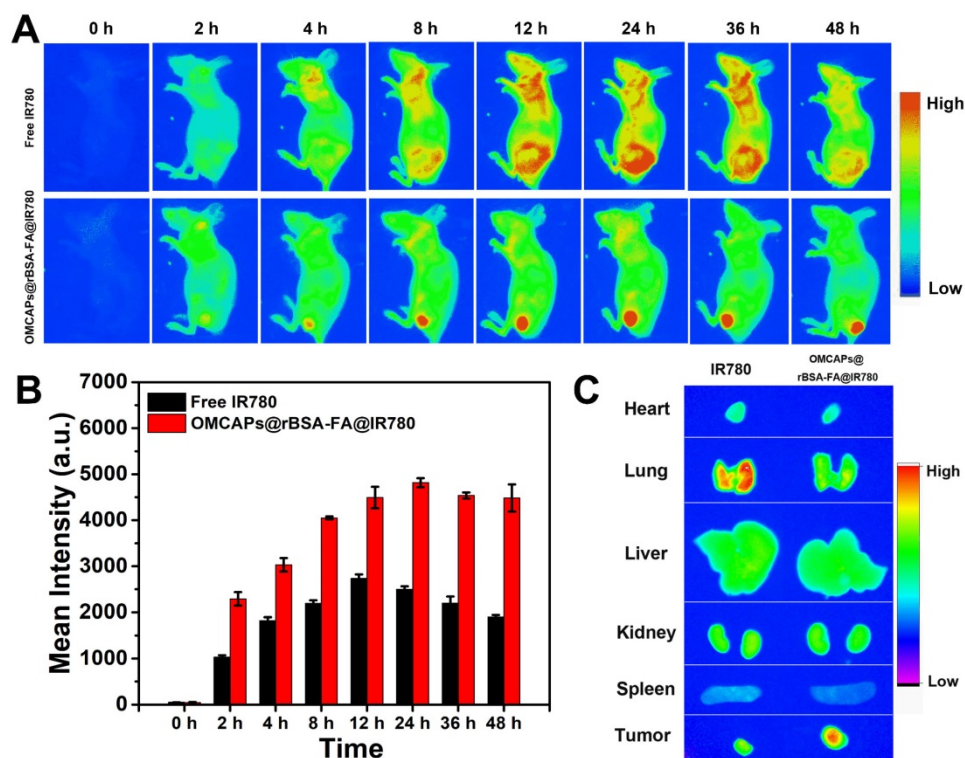
Figure 6. (A) *In vivo* fluorescence images of MGC803-tumor bearing mice after intravenous injection of free IR-780 and OMCAPs@rBSA-FA@IR780 at various time point (excitation: 710 nm; emission: 790 nm; integration time: 60 s). (B) The quantitative calculation of fluorescence intensity at tumor site over time. (C) The *ex vivo* fluorescence images of main organs and tumors from MGC803-tumor bearing mice after intravenous injection of free IR-780 and OMCAPs@rBSA-FA@IR780 after 48 h.

In vivo synergistically therapeutic effect of OMCAPs@rBSA-FA@IR780 in Tumor-Bearing Mice.

The *in vivo* therapeutic effect of OMCAPs@rBSA-FA@IR780 nanoprobes was further performed at MGC-803 tumor-bearing mice, which intravenously injected with PBS, free IR-780 or MCPs@rBSA-FA@IR780 (1 mg/kg of IR-780), respectively. After 24 h post-injection, the tumor site of mice was irradiation treated with 808 nm laser (1.0 W/cm², 5 min), and the temperature variation at tumor site from each group were monitored in real time. As displayed in Fig. 7A, the temperature in tumor site displayed a rising tendency with the increment of laser time. Among them, the temperature from free IR780 treated mice could reach to 49.1°C, while the one from nanoprobes treated mice obviously increased to 52.2 °C under same laser irradiation time, indicating that nanoprobes could induce irreversible tumor damage. However, the temperature of the PBS-treated tumor could only increase to 39.5 °C, which was insufficient to induce tumor thermal injury. In addition, the body weight changes and tumor volume increase in different groups of mice were investigated to monitor the therapy efficacy *in vivo*. As elucidated in Fig. 7B, in

absence of laser irradiation, the mice from all the groups exhibited almost same tumor growth rate and the relative tumor volume V/V_0 (V respected the growth volume, V_0 is the original tumor volume) were nearly increased to 6. Upon the laser irradiation, there was still a relatively rapid tumor growth rate in the PBS treated mice, and the IR780 group displayed a little tumor inhibition owing to the excellent PPT effect of IR780; notably, the group of OMCAPs@rBSA-FA@IR780 presented favorable tumor growth inhibition within 18 days, indicating the excellent PTT therapeutic effect.

Furthermore, as illustrated in Fig. S8, the tumor growth condition were also monitored by a camera to record the tumor changes of mice from different groups. The tumors are significantly growing over time in the groups including no laser treated groups and PBS group with laser irradiation. However, the tumor size of OMCAPs@rBSA-FA@IR780 treated mice under laser-irradiation had an atrophied tendency, and the tumor site showed obvious scar after 4 days. After 15 days, the tumor was almost ablated and normal tissue was regenerated in the OMCAPs@rBSA-FA@IR780 group with irradiation. Additionally, as shown in Fig. S11, the OMCAPs@rBSA-FA@IR780 treated mice recovered completely and there was no new tumor tissue

generated after 30 days. However, there was new tumor tissue appeared in the IR780 group after 15 days even though parts of tumor ablated, suggesting that the targeted effect of OMCAPs@rBSA-FA@IR780 could produce an abundant aggregation to enhance the therapy effect.

Additionally, the weight of mice from different groups was recorded to assess the therapy-induced toxic side effect. As displayed in Fig. 7C, no distinct body weight loss was observed in mice after treatment, proving that no significant adverse effect of the OMCAPs@rBSA-FA@IR780 nanoprobes.

H&E staining of main organs and tumors were further employed in this work to perform histopathological examination. As shown in Fig. 7D, all the groups did not show obviously pathological damage and abnormality in main organs, including heart, liver, spleen, lung and kidney. Likewise, the tumor of PBS treated mice displayed no obvious deterioration (in Fig. S9). However, the OMCAPs@rBSA-FA and IR780 groups partially damaged in the tumor region. Notably, most of cancer cells in the tumor site were destroyed treated by OMCAPs@rBSA-FA@IR780 nanoprobes under laser irradiation, with a result of a little size of tumor section. All above-mentioned result demonstrated that OMCAPs@rBSA-FA@IR780 nanoprobes based therapy strategy offered highly outstanding PTT ad PDT therapy effect without obvious side effects.

Conclusions

In this work, we successfully constructed carbon-gold hybrid nanocomposites (OMCAPs@rBSA-FA@IR780) acted as diagnostic and therapeutic probes, which possessed favorable targeting effect and excellent therapy effect combining PTT & PDT and nanozyme oxidative therapy for folate-overexpressed gastric cancer tumors. The developed OMCAPs@rBSA-FA@IR780 nanomaterials could not only be used to ablate tumor without generation after 30 days but also to perform NIR fluorescence imaging *in vitro* and *in vivo*. Interesting, well-protected Au NPs embedded in OMCAPs could act as nanozyme to catalyze H_2O_2 to produce •OH for synergetic cancer therapy. Moreover, the used OMCAPs were acted as carriers due to high loading rate reached to 33.3% and photothermal reagents as well to improve PTT therapy owing to efficient NIR light absorption. All above-showed results indicated this preliminary work might present an outstanding strategy for tumor therapy by assembling nanozyme catalysis, PTT and PDT treatment.

Methods

Materials

Gold chloride trihydrate ($HAuCl_4 \cdot 3H_2O$), formaldehyde (37 wt. %) and phenol were bought from Shanghai Titan Polytron Technologies Inc. (Shanghai, China). Pluronic F127 (Mw= 12,600, PEO106PPO70PEO106) was obtained from Acros Corp. In addition, hydrochloric acid (HCl, 37%), sulfuric acid (H_2SO_4, 98%), nitric acid (HNO₃, ≥97.2), folic acid (FA), anhydrous dimethyl sulfoxide (DMSO) and sodium borohydride (NaBH₄) were all
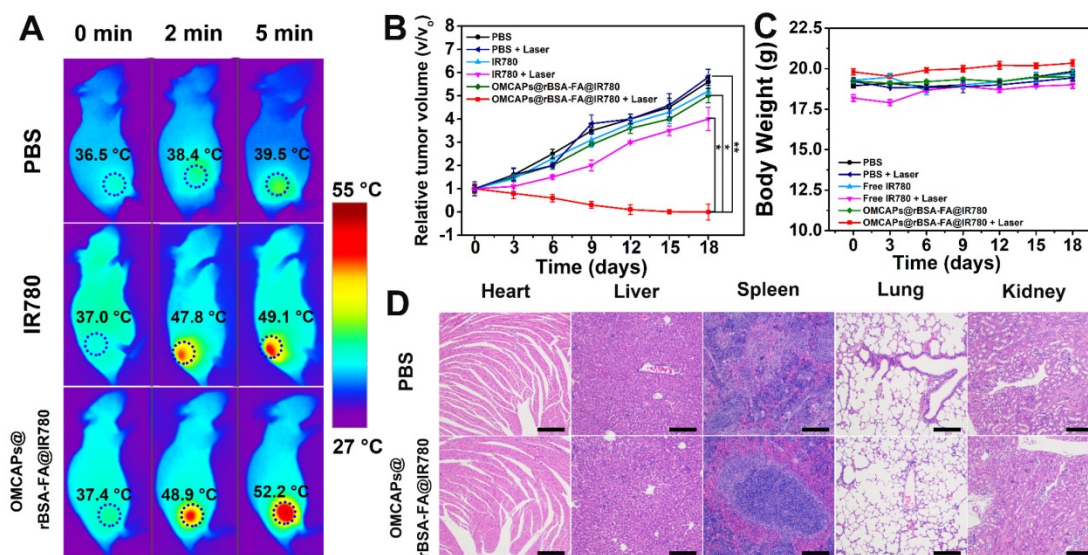

Figure 7. (A) Infrared thermographic mapping of mice treated with PBS, free IR-780 and OMCAPs@rBSA-FA@IR780 to reveal temperature variation in the tumor site under laser irradiation with the power density of 1.0 W/cm² at 808 nm. (B) Curves of relative tumor volume change for various materials treated mice including PBS, free IR780 and OMCAPs@rBSA-FA@IR780 with or without irradiation. (n=5, *P < 0.05, **P < 0.01). (C) Body weight fluctuation curves of different materials treated mice in presence/absence of laser irradiation. (D) Histopathological examination of the mice's organs that post-injected with PBS and OMCAPs@rBSA-FA@IR780 respectively after 18 days (Hematoxylin and eosin (H&E) staining). Scale bar: 200 μm.

purchased from Sinopharm Chemical Reagent Co. Ltd. (Shanghai, China). N-hydroxysuccinimide (NHS), bovine serum albumin (BSA, 99.9%) and N-(3-dimethylaminopropyl)-N′-ethylcarbodiimide hydrochloride (EDC) were obtained from Aladdin Reagent Co., Ltd. (Shanghai, China). Annexin V-FITC/PI Apoptosis Detection Kit, 2-(4-Amidinophenyl)-6-indolecarbamidine dihydrochloride (DAPI), Cell Counting Kit (CCK-8) and Calcein-AM/PI Double Stain Kit were all bought from YEASEN Corporation (Shanghai, China). Fetal bovine serum (FBS), Dulbecco's Modified Eagle's Medium (DMEM), Penicilline Streptomycin and Trypsine EDTA used for cell culture were all obtained from Gibco Life Technologies. All chemical reagents used here were of analytical grade without further purification. The double-distilled water (18.2 MΩ, Millipore Co., USA) was employed in all experiments. In addition, phosphate buffered solutions (PBS, 0.1 M) were acquired by using 0.1 M Na_2HPO_4 and 0.1 M KH_2PO_4.

Preparation of MCAPs and OMCAPs

The MCAPs acted as carriers and photothermal reagents were synthesized according to a hydrothermal method with a slight modification [49]. In brief, 0.6 g phenol, 2.1 mL formalin aqueous solution (37 wt.%) and 15 mL 0.1 M NaOH were firstly mixed with stirring in a 100 mL round-bottom flask at 70 °C. After heating for 30 min with magnetic stirring, pluronic F127 aqueous solution (7.4 wt. %, 16.2 g) was added and changed reaction temperature to 66 °C for another 3 h stirring. Then, a solution containing 0.128 g 3-mercaptopropyltrimethoxysilane (MPTMS, 98 wt.% Acros Chemical Inc.), 150 µL $HAuCl_4$ (242.81 mM) and 50 mL pure water were added into the above-mixture for about 12-18 h. When deposition appeared, the reaction should be immediately finished and quiescence for a period of time until the deposits dissolved. The obtained solution was then diluted with deionized water with a ratio of 177/560 (v/v), and following transferred into the autoclave with heating at 130 °C for 24 h. Afterwards, the centrifuged-acquired yellow products were washed with water and ethanol in succession for several times to remove impurities. Finally, the products were dried and then heated at 700 °C for 3 h under the protection of nitrogen gas flow in order to remove F127 and carbonize resins, with a result of pure black products MCAPs.

In order to improve hydrophily of MCAPs, the mixed strong acid including H_2SO_4 (18 mL, 98%) and HNO_3 (6 mL, 70%) were used to oxidize 40 mg MCAPs with 5 h sonication at ambient temperature, resulting numerous carboxyl groups generated at the surface of MCAPs. After that, carboxylated MCAPs (OMCAPs) were washed with diluted HCl (4%) and water successively four times to remove the impurity substance. Finally, above-obtained carboxylated MCAPs were dried at 60 °C for overnight.

Synthesis procedure of rBSA-FA functionalization of OMCAPs

Synthesis of OMCAPs@rBSA-FA was divided into the following three steps: (i) FA activation; (ii) synthesis of rBSA; (iii) rBSA-FA conjugation; (iv) rBSA-FA functionalized OMCAPs. The target molecule FA was activated to form activated FA (FA-NHS) according to our previous works [50, 51]. Briefly, 1g FA was dissolved in 50 mL anhydrous DMSO. Then, 1.05 g EDC·HCl and 0.632 g NHS (molar ratio of FA/EDC/NHS = 1:2.5:2.5) were added into above-solution, and the system was reacted in the dark at ambient temperature for 12 h with gently stirring. After removing the insoluble byproduct (dicyclohexylurea) by centrifugation, the FA-NHS solution was deposited by adding the mixture of cold acetone and diethylether (v/v=3/7) and collected. Then, the obtained precipitate was washed several times with acetone/diethylether by resuspending and centrifugation in turn. Finally, activated FA was freeze-dried. Meantime, reduced serum albumin (rBSA) was synthesized by following way. At first, freshly prepared $NaBH_4$ (1 M, 250 µL) was added into BSA solution (2 mg/mL, 20 mL) with 2 h stirring reaction. Then, 40 mg FA-NHS was reacted with the rBSA solution with stirring for another 4 h reaction to obtain rBSA-FA composites. The obtained product was purified by centrifugal ultrfiltration (Amicin Ultr-15, Millipore, 3 K MWCO) and dried by a vacuum freeze-drying. To synthesize rBSA-FA functionalized OMCAPs, 2 mg carboxylated MCAPs were dissolved into 2 mL PBS (pH=7.4, 0.1M) with adding 2 mg EDC, 2 mg NHS and 2 mg rBSA-FA. After 6 h reaction with stirring at room temperature, the lastly obtained rBSA-FA functionalized OMCAPs (OMCAPs@rBSA-FA) were centrifuged and washed with water for three times. Ultimately, OMCAPs@rBSA-FA were freeze-dried for further use.

Fabrication of OMCAPs@ rBSA-FA@IR780 nanoprobes

IR780 molecules were loaded into OMCAPs@rBSA-FA to fabricate OMCAPs@rBSA-FA@IR780 nanoprobes. In detail, 4 mg/mL of IR780 dissolved in DMSO was added into above-prepared OMCAPs@rBSA-FA solution (2 mg/mL) for 8 h reaction with shaking at 37 °C. To remove unreacted chemical reagents, final resultant was washed three times with PBS (pH 7.4, 0.1 M) by centrifugation at

9000 rpm and redispeared by sonication in turn. In addition, the centrifugal supernatant solution was collected to calculate the amount of unloaded IR780. Ultimately, the purified OMCAPs@ rBSA-FA@IR780 was dissolved into 1 mL PBS (pH 7.4, 0.1 M) for the subsequent application.

The IR780 entrapment efficiency (EE) and loading rate (LR) were calculated based on the following equations:

$$EE(\%) = \frac{Weight\ of\ IR780\ in\ nanoprobes}{Weight\ of\ IR780\ added\ initially} \times 100\%$$

$$LR(\%)$$
$$= \frac{Weight\ of\ IR780\ in\ nanoprobes}{Weight\ of\ IR780 + Weight\ of\ OMCAPs@rBSA - FA}$$
$$\times 100\%$$

Characterization of various materials

The morphology and structure of various nanomaterials were studied by field emission transmission electron microscopy (FE-TEM, Talos F200X) and scanning electron microscopy (SEM, Zeiss Ultra5). The hydrodynamic sizes of different NPs were investigated by dynamic light scattering (DLS, Nano Brook Omni Zeta/PLS, Brook, USA). The UV-vis spectrophotometer (Varian Inc., Palo Alto, CA, USA) was used to study the modified information of probes. In addition, Fourier transform infrared spectroscopy (FTIR) of different nanomaterials were carried out on a Fourier transform infrared spectrometer (Nicolet 6700).

Cell lines and culture conditions

The man gastric cancer cells (MGC-803) were cultured in DMEM with the addition of 10% (v/v) fetal bovine serum, 100 U/mL penicillin and 0.1 mg/mL streptomycin (named as complete medium) at 37 °C and 5% CO_2. Moreover, the cells were selected for use in experiment when they were in the logarithmic growth phase. Trypsin/EDTA were employed to subculture MGC-803 cells.

Peroxidase-like enzymatic catalysis ability of OMCAPs and OMCAPs@rBSA-FA

The main UV-Vis absorbance peaks of oxidized TMB were recorded in presence of OMCAPs or OMCAPs @rBSA with H_2O_2 in NaAc buffer (0.1 M, pH 6.0). Herein, 1.0 mL buffer solution was used to dissolve various kinds of catalysis materials (10 µg/mL), TMB (0.416 mM) and H_2O_2 (final concentration 100 µM). Then, the obtained reaction systems were carried out by using UV-vis spectrophotometer to study the enzymatic catalysis ability of OMCAPs and OMCAPs@rBSA-FA.

Hydroxyl radical (·OH) determination

The detection of generated ·OH was using the reaction between terephthalic acid (TA) and ·OH by following a method reported previously [52]. TA could effectively react with ·OH to generate 2-hydroxy terephthalic acid, which could exhibit unique fluorescence around 435 nm (λ_{ex}: 315 nm) while the TA with negligible fluorescence. In brief, 1.0 mL of NaAc buffer (0.1 M, pH 6.0) was used to dissolve various kinds of catalysis materials (50 µg/mL) and H_2O_2 (final concentration: 100 µM). After 3 min incubation, 1 mL of terephthalic acid (4 mM, 10 mM NaOH used as solvent) was added into about mixture for another 20 min reaction with shaking. Finally, the obtained reaction systems were performed on a fluorescent spectrophotometer.

Singlet oxygen determination

The singlet oxygen sensor green (SOSG) regent could be regarded as an effective tool to measure $^1O_2$ generated from free IR780 (50 µg/mL) and OMCAPs@ rBSA-FA@IR780 (equivalent 50 µg/mL IR780) to exhibit the PDT ability of our finally acquired nanoprobes. In this work, the concentration of SOSG was 2.5×10^{-6} M and the generation of $^1O_2$ could be observed by recording the SOSG fluorescence (λ_{ex}: 494 nm).

Cytotoxicity of various materials

Cytotoxicity study is a key step in assessing the toxicity of developed probe for its further biomedical applications and evaluating the therapeutic efficacy. Herein, CCK-8 Assays, Calcein-AM and PI Staining Assay as well as Apoptosis Assay were all used to assess the dark toxicity and phototoxicity of various materials containing free IR780, OMCAPs@ rBSA-FA and OMCAPs@ rBSA-FA@IR780 nanoprobes.

CCK-8 Assay. In brief, MGC-803 cells (5×10^3 per well) were seeded in 96-cell plates with a 24 h incubation. Then, the cells were following incubated with 100 µL fresh complete medium containing IR780, OMCAPs@rBSA-FA and OMCAPs@rBSA-FA@IR780 at different concentrations (IR780 dosage: 1- 6 µg/mL, OMCAPs@rBSA-FA dosage: 2 -12 µg/mL) for 12 h endocytosis. In addition, the control groups were the cells blankly treated with 100 µL of fresh complete medium. After rinsed with PBS twice, the cells were replaced with fresh complete medium. Following that, the obtained cells in per well were treated with or without a 1.0 W/cm^2 808 nm laser radiation for 5 min. After another 12 h incubation in the dark, cells' viability with different treatments were measured by CCK-8 assay and quantified on Microplate Reader with an absorbance peak at 450 nm. The acquired data were dealt with followed formula:

$$Cell\ viability = \frac{OD_{Treated} - OD_{Blank}}{OD_{Control} - OD_{Blank}}$$

Apoptosis Assay. Apoptosis situation was investigated on a BD FACSCalibur (BD Biosciences, Mountain View, CA) after the apoptotic and necrotic cells were treated with Annexin V-FITC/PI Apoptosis Detection Kit (Yeasen, Shanghai). In brief, MGC-803 cells (1×10^5 cells per well) were firstly incubated in 6-cell plates for 24 h growth and then respectively treated with IR780, OMCAPs@rBSA-FA and OMCAPs@rBSA-FA@IR780 (the same concentrations as CCK-8 assay) for another 12 h incubation. After the cells were changed with fresh medium, the cells were treated with or without 1.0 W/cm^2 808 nm laser radiation for 5 min. After an extra 12 h incubation, the cells were trypsinized, centrifuged, washed with PBS and resuspended in 400 µL of binding buffer containing 5 µL of Annexin V and 10 µL of PI. After 10 min staining of cells, the obtained solution including cells was investigated by flow cytometry and the acquired data were studied with FlowJo 10.0 software.

Calcein-AM and PI Staining Assay. To visually verify therapeutic efficacy of different materials, the cells were stained and observed by a fluorescence microscope. At first, the MGC-803 cells (1.0×10^4 cells per well) were seeded in 24-cell plates for 24 h incubation. Then, the original medium was changed with competing medium including PBS, free IR780 (6 µg/mL) and final nanoprobes (6 µg/mL IR780) respectively for 12 h incubation. After replacement by fresh medium, the cells were irradiated with or without NIR laser (808 nm, 1 W/cm^2) for 5 min. After 12 h incubation, the cells were washed with PBS and stained with calcein-AM (2.0 µM) and PI (1.5 µM). Finally, the stained cells were observed by fluorescence microscope.

Cellular Uptake Assay of various materials

Confocal microscopy and flow cytometry could be used to study cellular uptake by a qualitative and quantitative way in respective. For confocal microscopy experiments, MGC-803 cells were seeded in 14 mm glass coverslips and cultured for 24 h. After interacted with free IR780 (6 µg/mL) and OMCAPs@rBSA-FA@IR780 (6 µg/mL IR780) for 1, 4 and 12 h, respectively, the cells were rinsed with PBS gently and fixed with 4% paraformaldehyde for 30 min at 37 °C. Following rinsed with PBS, the nucleus of cells were stained with 4′, 6-diamidino-2-phenylindole (DAPI) for 5 min in dark. After washed with PBS sufficiently to remove redundant DAPI, the stained cells were observed on a Leica TCS SP8 confocal laser scanning microscopy. In addition, DAPI was excited with 405 nm excitation light and the corresponding emission was recorded from 440 to 470 nm. The excitation wavelength of IR780 of nanoprobes was 633

nm and emission was collected from 700 to 800 nm.

For flow cytometry experimentation, MGC-803 cells (1.0×10^5 cells per well) were incubated in 6-well plates for 12 h. After incubated with free IR780 (6 µg/mL) and OMCAPs@ rBSA-FA@IR780 (6 µg/mL IR780) for various times (the same time point as confocal microscopy), the cells were trypsinized, washed with PBS buffer and resuspended in 1 mL PBS for flow cytometry measurements to validate the cellular uptake efficiency. Additionally, the fluorescence signal of FL3-H channel was collected to exhibit the intensity of IR780.

Animals and tumor model

Shanghai Jiesijie Laboratory Animal Co. Ltd. (China) provided female nude mice in 6 weeks' old and 18~22 g. All mice were carefully raised according to the guidelines provided by Approval of institutional Animal Care and Use Committee of Shanghai Jiao Tong University. In order to setup gastric cancer tumor model, MGC-803 cells with a concentration of 2×10^6 in 50 µL saline were subcutaneous injected into the right flank of isoflurane-anesthetized mice. When the size of the established tumor reached to about 100 mm^3, the mice were ready for *in vivo* and ex-vivo experiment.

In vivo and *ex vivo* NIR fluorescence imaging

To *in vivo* monitor the distribution and targeted efficacy of constructed OMCAPs@ rBSA-FA@IR780 probes, NIR fluorescence imaging was used to investigate the distribution of free IR780 and naocomposites. For fluorescence imaging *in vivo*, 100 µL of free IR-780 in PBS and OMCAPs@rBSA-FA@IR780 (IR780 content: 5 mg/kg) were intravenously injected to the corresponding mice. In addition, the fluorescence images of mice at different time point were recorded by a Bruker In-Vivo F PRO imaging system (Billerica, MA, USA) with 720/20 nm excitation and 790/30 nm emission at 60 s exposure time. Ultimately, the mice were sacrificed at 48 h and the organs (heart, liver, spleen, lung and kidney) and tumor were imaged at the same parameters as *in vivo* imaging. A Bruker Molecular Imaging Software was used to calculate the average fluorescence intensity of different parts.

In vivo therapy effect of mice tumor

The MGC-803 tumor-bearing mice were firstly intravenously injected with 100 µL of PBS (acted as control), free IR-780 and OMCAPs@ rBSA-FA@IR780 (IR780 content: 5 mg/kg), respectively. After 24 h post-injection, the tumor sites were treated with 1.0 W/cm^2 808 nm laser radiation for 5 min. In the meantime, the temperature changes at the tumor sites and the infrared pictures were recorded by utilizing

an infrared camera. Afterwards, the relative tumor volume and mice weight were measured every 3 days within 18 days, and the changes of tumor sites from each group have been recorded every day by a camera. After 18 days' therapy, the organs included heart, liver, spleen, lung and kidney were taken out and stained with hematoxylin and eosin (H&E) and the corresponding morphological features were studied to show the side effect of our probe compared with PBS group.

Statistical Analysis

All results demonstrated in this work were reported as means ± SD.

Abbreviations

Au NPs: gold nanoparticles; OMCAPs: carboxylated mesoporous carbon-gold hybrid; MCAPs: mesoporous carbon-gold hybrid; CNT: carbon nanotubes; GO: graphene oxide; MCNs: mesoporous carbon nanospheres; CNPs: carbon nanospheres; NIR: near-infrared; PTT: photo-thermal therapy; PDT: photodynamic therapy; ROS: reactive oxygen species; $HAuCl_4\ 3H_2O$: gold chloride trihydrate; HCl: hydrochloric acid; H_2SO_4: sulfuric acid; HNO_3: nitric acid; FA: folic acid; DMSO: anhydrous dimethyl sulfoxide; $NaBH_4$: sodium borohydride; NHS: N-hydroxysuccinimide; BSA: bovine serum albumin; N-(3-dimethylaminopropyl)-EDC: N′-ethylcarbodiimide hydrochloride; DAPI: 2-(4-Amidinophenyl)-6-indolecarbamidine dihydrochloride; CCK-8: cell Counting Kit; MPTMS: 3-mercaptopropyltrimethoxysilane; FA-NHS: activated FA; TMB: tetramethylbenzidine; HRP: horseradish peroxidase; TA: terephthalic acid.

Supplementary Material

Supplementary data including characterization of BSA, FA and rBSA-FA, UV-vis spectra of IR780, tumor images of various materials treated mice, picture of mice treated after 30 days.
http://www.thno.org/v09p3443s1.pdf

Acknowledgements

Competing Interests

The authors have declared that no competing interest exists.

References

1. Yue C, Liu P, Zheng M, Zhao P, Wang Y, Ma Y, et al. IR-780 dye loaded tumor targeting theranostic nanoparticles for NIR imaging and photothermal therapy. Biomaterials. 2013; 34: 6853-61.
2. Lin T, Yuan A, Zhao X, Lian H, Zhuang J, Chen W, et al. Self-assembled tumor-targeting hyaluronic acid nanoparticles for photothermal ablation in orthotopic bladder cancer. Acta Biomater. 2017; 53: 427-38.
3. Zhang L, Wang D, Yang K, Sheng D, Tan B, Wang Z, et al. Mitochondria-Targeted Artificial "Nano-RBCs" for Amplified Synergistic Cancer Phototherapy by a Single NIR Irradiation. Adv Sci (Weinh). 2018; 5: 1800049.
4. Chen Q, Liu X, Zeng J, Cheng Z, Liu Z. Albumin-NIR dye self-assembled nanoparticles for photoacoustic pH imaging and pH-responsive photothermal therapy effective for large tumors. Biomaterials. 2016; 98: 23-30.
5. Li J, Zhen X, Lyu Y, Jiang Y, Huang J, Pu K. Cell Membrane Coated Semiconducting Polymer Nanoparticles for Enhanced Multimodal Cancer Phototheranostics. ACS Nano. 2018; 12: 8520-30.
6. Jiang Y, Li J, Zhen X, Xie C, Pu K. Dual-Peak Absorbing Semiconducting Copolymer Nanoparticles for First and Second Near-Infrared Window Photothermal Therapy: A Comparative Study. Adv Mater. 2018; 30: e1705980.
7. Zhen X, Zhang J, Huang J, Xie C, Miao Q, Pu K. Macrotheranostic Probe with Disease-Activated Near-Infrared Fluorescence, Photoacoustic, and Photothermal Signals for Imaging-Guided Therapy. Angew Chem Int Ed Engl. 2018; 57: 7804-8.
8. Zhen X, Xie C, Pu K. Temperature-Correlated Afterglow of a Semiconducting Polymer Nanococktail for Imaging-Guided Photothermal Therapy. Angew Chem Int Ed Engl. 2018; 57: 3938-42.
9. Jiang W, Zhang H, Wu J, Zhai G, Li Z, Luan Y, et al. CuS@MOF-Based Well-Designed Quercetin Delivery System for Chemo-Photothermal Therapy. ACS Appl Mater Interfaces. 2018; 10: 34513-23.
10. Zhang D, Zhang J, Li Q, Tian H, Zhang N, Li Z, et al. pH- and Enzyme-Sensitive IR820-Paclitaxel Conjugate Self-Assembled Nanovehicles for Near-Infrared Fluorescence Imaging-Guided Chemo-Photothermal Therapy. ACS Appl Mater Interfaces. 2018; 10: 30092-102.
11. Zhang H, Li Q, Liu R, Zhang X, Li Z, Luan Y. A Versatile Prodrug Strategy to *In situ* Encapsulate Drugs in MOF Nanocarriers: A Case of Cytarabine-IR820 Prodrug Encapsulated ZIF-8 toward Chemo-Photothermal Therapy. Adv Funct Mater. 2018; 28: 1802830.
12. Pais-Silva C, de Melo-Diogo D, Correia IJ. IR780-loaded TPGS-TOS micelles for breast cancer photodynamic therapy. Eur J Pharm Biopharm. 2017; 113: 108-17.
13. Hou W, Zhao X, Qian X, Pan F, Zhang C, Yang Y, et al. pH-Sensitive self-assembling nanoparticles for tumor near-infrared fluorescence imaging and chemo-photodynamic combination therapy. Nanoscale. 2016; 8: 104-16.
14. Li Y, Wen T, Zhao R, Liu X, Ji T, Wang H et al. Localized Electric Field of Plasmonic Nanoplatform Enhanced Photodynamic Tumor Therapy. ACS Nano. 2014; 8: 11529-42.
15. Hu X, Tian H, Jiang W, Song A, Li Z, Luan Y. Rational Design of IR820- and Ce6-Based Versatile Micelle for Single NIR Laser-Induced Imaging and Dual-Modal Phototherapy. Small. 2018; 14: 1802994.
16. Li J, Pu K. Development of organic semiconducting materials for deep-tissue optical imaging, phototherapy and photoactivation. Chem Soc Rev. 2019; 48: 38-71.
17. Zhu H, Li J, Qi X, Chen P, Pu K. Oxygenic Hybrid Semiconducting Nanoparticles for Enhanced Photodynamic Therapy. Nano Lett. 2018; 18: 586-94.
18. Zhu H, Fang Y, Miao Q, Qi X, Ding D, Chen P, et al. Regulating Near-Infrared Photodynamic Properties of Semiconducting Polymer Nanotheranostics for Optimized Cancer Therapy. ACS Nano. 2017; 11: 8998-9009.
19. Zha Z, Yue X, Ren Q, Dai Z. Uniform polypyrrole nanoparticles with high photothermal conversion efficiency for photothermal ablation of cancer cells. Adv Mater. 2013; 25: 777-82.
20. Hou W, Xia F, Alves CS, Qian X, Yang Y, Cui D. MMP2-Targeting and Redox-Responsive PEGylated Chlorin e6 Nanoparticles for Cancer Near-Infrared Imaging and Photodynamic Therapy. ACS Appl Mater Interfaces. 2016; 8: 1447-57.
21. Zhang C, Wang S, Xiao J, Tan X, Zhu Y, Su Y, et al. Sentinel lymph node mapping by a near-infrared fluorescent heptamethine dye. Biomaterials. 2010; 31: 1911-7.
22. Manea F, Houillon FB, Pasquato L, Scrimin P. Nanozymes: Gold-Nanoparticle-Based Transphosphorylation Catalysts. Angewandte Chemie. 2004; 116: 6291-5.
23. Wang X, Hu Y, Wei H. Nanozymes in bionanotechnology: from sensing to therapeutics and beyond. Inorg Chem Front. 2016; 3: 41-60.
24. Wu J, Li S, Wei H. Multifunctional nanozymes: enzyme-like catalytic activity combined with magnetism and surface plasmon resonance. Nanoscale Horiz. 2018; 3: 367-82.
25. Wei H, Wang E. Nanomaterials with enzyme-like characteristics (nanozymes): next-generation artificial enzymes. Chem Soc Rev. 2013; 42: 6060-93.
26. Wei J, Li J, Sun D, Li Q, Ma J, Chen X, et al. A Novel Theranostic Nanoplatform Based on Pd@Pt-PEG-Ce6 for Enhanced Photodynamic Therapy by Modulating Tumor Hypoxia Microenvironment. Adv Funct Mater. 2018; 28: 1706310.

27. Qu F, Li T, Yang M. Colorimetric platform for visual detection of cancer biomarker based on intrinsic peroxidase activity of graphene oxide. Biosens Bioelectron. 2011; 26: 3927-31.

28. Lyu Y, Tian J, Li J, Chen P, Pu K. Semiconducting Polymer Nanobiocatalysts for Photoactivation of Intracellular Redox Reactions. Angew Chem Int Ed Engl. 2018; 57: 13484-8.

29. Li J, Xie C, Huang J, Jiang Y, Miao Q, Pu K. Semiconducting Polymer Nanoenzymes with Photothermic Activity for Enhanced Cancer Therapy. Angew Chem Int Ed Engl. 2018; 57: 3995-8.

30. Zhao M, Deng K, He L, Liu Y, Li G, Zhao H, et al. Core-shell palladium nanoparticle@metal-organic frameworks as multifunctional catalysts for cascade reactions. J Am Chem Soc. 2014; 136: 1738-41.

31. Liu J, Meng LJ, Fei ZF, Dyson PJ, Jing XN, Liu X. MnO2 nanosheets as an artificial enzyme to mimic oxidase for rapid and sensitive detection of glutathione. Biosens Bioelectron. 2017; 90: 69-74.

32. Lin Y, Ren J, Qu X. Nano-gold as artificial enzymes: hidden talents. Adv Mater. 2014; 26: 4200-17.

33. He W, Zhou YT, Wamer WG, Hu X, Wu X, Zheng Z, et al. Intrinsic catalytic activity of Au nanoparticles with respect to hydrogen peroxide decomposition and superoxide scavenging. Biomaterials. 2013; 34: 765-73.

34. Comotti M, Della Pina C, Matarrese R, Rossi M. The catalytic activity of "naked" gold particles. Angew Chem Int Ed Engl. 2004; 43: 5812-5.

35. Du X, Zhao C, Zhou M, Ma T, Huang H, Jaroniec M, et al. Hollow Carbon Nanospheres with Tunable Hierarchical Pores for Drug, Gene, and Photothermal Synergistic Treatment. Small. 2017; 13: 1602592.

36. Zhou L, Jing Y, Liu Y, Liu Z, Gao D, Chen H, et al. Mesoporous Carbon Nanospheres as a Multifunctional Carrier for Cancer Theranostics. Theranostics. 2018; 8: 663-75.

37. Wang X, Liu Y, Liu Z, Hu J, Guo H, Wang F. Synergistic chemo-photothermal therapy of tumor by hollow carbon nanospheres. Biochem Biophys Res Commun. 2018; 495: 867-72.

38. Zhu J, Liao L, Bian X, Kong J, Yang P, Liu B. pH-controlled delivery of doxorubicin to cancer cells, based on small mesoporous carbon nanospheres. Small. 2012; 8: 2715-20.

39. Karavasili C, Amanatiadou EP, Sygellou L, Giasafaki DK, Steriotis TA, Charalambopoulou GC, et al. Development of new drug delivery system based on ordered mesoporous carbons: characterisation and cytocompatibility studies. J Mater Chem B. 2013; 1: 3167.

40. Trifonov A, Herkendell K, Tel-Vered R, Yehezkeli O, Woerner M, Willner I. Enzyme-Capped Relay-Functionalized Mesoporous Carbon Nanoparticles: Effective Bioelectrocatalytic Matrices for Sensing and Biofuel Cell Applications. Acs Nano. 2013; 7: 11358-68.

41. Fang Y, Gu D, Zou Y, Wu Z, Li F, Che R, et al. A low-concentration hydrothermal synthesis of biocompatible ordered mesoporous carbon nanospheres with tunable and uniform size. Angew Chem Int Ed Engl. 2010; 49: 7987-91.

42. Gu J, Su S, Li Y, He Q, Shi J. Hydrophilic mesoporous carbon nanoparticles as carriers for sustained release of hydrophobic anti-cancer drugs. Chem Commun (Camb). 2011; 47: 2101-3.

43. Chen Y, Xu P, Wu M, Meng Q, Chen H, Shu Z, et al. Colloidal RBC-shaped, hydrophilic, and hollow mesoporous carbon nanocapsules for highly efficient biomedical engineering. Adv Mater. 2014; 26: 4294-301.

44. Fan L, Xu X, Zhu C, Han J, Gao L, Xi J, et al. Tumor Catalytic-Photothermal Therapy with Yolk-Shell Gold@Carbon Nanozymes. ACS Appl Mater Interfaces. 2018; 10: 4502-11.

45. Chen Y, Song B, Li M, Lu L, Xue J. Fe3O4 Nanoparticles Embedded in Uniform Mesoporous Carbon Spheres for Superior High-Rate Battery Applications. Adv Funct Mater. 2014; 24: 319-26.

46. Hu D, Chen L, Qu Y, Peng J, Chu B, Shi K, et al. Oxygen-generating Hybrid Polymeric Nanoparticles with Encapsulated Doxorubicin and Chlorin e6 for Trimodal Imaging-Guided Combined Chemo-Photodynamic Therapy. Theranostics. 2018; 8: 1558-74.

47. Xu G, Liu S, Niu H, Lv W, Wu Ra. Functionalized mesoporous carbon nanoparticles for targeted chemo-photothermal therapy of cancer cells under near-infrared irradiation. RSC Adv. 2014; 4: 33986-97.

48. Wang H, Wang K, Mu Q, Stephen ZR, Yu Y, Zhou S, et al. Mesoporous carbon nanoshells for high hydrophobic drug loading, multimodal optical imaging, controlled drug release, and synergistic therapy. Nanoscale. 2017; 9: 1434-42.

49. Fu H, Zhang L, Wang Y, Chen S, Wan Y. Thermally reduced gold nanocatalysts prepared by the carbonization of ordered mesoporous carbon as a heterogeneous catalyst for the selective reduction of aromatic nitro compounds. J Catal. 2016; 344: 313-24.

50. Zhang C, Li C, Liu Y, Zhang J, Bao C, Liang S, et al. Gold Nanoclusters-Based Nanoprobes for Simultaneous Fluorescence Imaging and Targeted Photodynamic Therapy with Superior Penetration and Retention Behavior in Tumors. Adv Funct Mater. 2015; 25: 1314-25.

51. Zhang C, Zhou Z, Qian Q, Gao G, Li C, Feng L, et al. Glutathione-capped fluorescent gold nanoclusters for dual-modal fluorescence/X-ray computed tomography imaging. J Mater Chem B. 2013; 1: 5045.

52. Wang Z, Zhang Y, Ju E, Liu Z, Cao F, Chen Z, et al. Biomimetic nanoflowers by self-assembly of nanozymes to induce intracellular oxidative damage against hypoxic tumors. Nat Commun. 2018; 9: 3334.